Influence of lower sheet material strength on joint quality in self-piercing riveting

Nguyen Hoang[1], Tran Duy Thong[1], Pham Quang Anh[1], Tran Dinh Van[1, 2], Pham Quoc Tuan[1*], Dinh Van Duy[1], Nguyen Dac Trung[1]

[1]School of Mechanical Engineering, Hanoi University of Science and Technology, 1 Dai Co Viet, Bach Mai, Hanoi, Vietnam;
[2]East Asia University of Technology, Phan Tay Nhac, Xuan Phuong, Hanoi, Vietnam.
[*]Corresponding author: tuan.phamquoc@hust.edu.vn
Received 28 Dec. 2025; Revised 8 Feb. 2026; Accepted 10 Feb. 2026; Published 25 Feb. 2026.
DOI: https://doi.org/10.54939/1859-1043.j.mst.109.2026.164-174

ABSTRACT

Self-piercing riveting (SPR) has become a key joining technique for lightweight and high-strength joints, especially in the automotive and aerospace industries. This study investigates how the strength of the lower sheet affects the performance of SPR joints. While the upper sheet remains unchanged, the lower sheet varies using various alloys (AA7075-F, AA2019, BA0270, Mat A, and Mat B). A finite element model developed in Abaqus/Explicit was employed to simulate the SPR process and assess joint performance. Key joint evaluation criteria, such as interlock and remaining thickness, are also discussed. The results indicate that the strength of the lower sheet must reach a certain threshold to ensure proper joint formation. While increasing the lower sheet's strength can enhance joint quality, excessive material strength may yield an insufficient interlock within the material or even generate a failure of the lower sheet.

Keywords: Self-piercing riveting; Finite element analysis; Joining capability; Sheet metals; Virtual material.

1. INTRODUCTION

The manufacturing industry increasingly demands efficient and sustainable joining methods, particularly in automotive and aerospace sectors, where lightweight multi-material assemblies are essential for performance and energy efficiency [1, 2]. Self-piercing riveting (SPR) has emerged as an advanced cold-forming technique producing robust mechanical interlocks without pre-drilled holes or thermal distortion [3-5]. Unlike welding, SPR preserves base material integrity and enables reliable joining of dissimilar combinations such as aluminum–steel, while offering enhanced fatigue resistance and mechanical performance [6-9].

Finite element (FE) simulations are crucial for understanding and optimizing the SPR process [10-13]. In these models, the rivet and metallic sheets are typically simulated as elastoplastic deformable bodies, while the punch, blank holder, and die are assumed to be rigid bodies. Due to the axisymmetric nature of the SPR process around the rivet center, two-dimensional axisymmetric models can be employed to reduce computational time and cost [14, 15]. However, the complex geometry of the rivet and die, the large number of contact surfaces, and the need to model failure mechanisms pose significant challenges. Various damage modeling approaches have been implemented, including deformation-based and material failure criteria [10, 11]. Some methods impose a maximum deformation threshold at the FE level, but their accuracy depends on the mesh refinement [12]. Others rely on stress-based failure criteria to determine the extent of material damage [13]. Numerical simulations of different design configurations allow for the evaluation of joint feasibility and quality without requiring extensive experimental trials, which are both costly and inefficient [14]. It should be noted that both joint feasibility and joint quality are assessed based on the achieved interlock distance, which is influenced by material properties and the geometric characteristics of the die components. Notably, variations in rivet geometry can significantly impact the riveting process, largely determining the joint characteristics. However, to accurately assess the

importance of individual parameters and identify optimal material and design configurations, a parametric analysis must be conducted across a wide range of design components.

Despite its advantages, achieving a high-quality SPR joint requires precise control of several key parameters, including rivet geometry, punch force, and material properties [16-18]. Improper parameter selection can lead to defects such as incomplete interlock formation, excessive sheet deformation, or premature failure under loading conditions [6]. Therefore, understanding the fundamental mechanics of SPR and optimizing its process parameters is critical to ensuring long-term reliability and durability of the joint [19, 20]. The material property of the joined metal sheet is also a critical factor that directly affects the formation and quality of the joint. Abe et al. studied the joining capability of aluminum and steel [8]. Their results indicated that the top sheet needed to be thinner than the lower sheet to form a successful joint. However, this finding applied to older SPR systems, whereas modern SPR systems can still create joints even when the top sheet is thicker than the lower sheet [21]. Chung and Kim [21] investigated the fatigue performance of SPR joints between aluminum and mild steel. They used sheets of equal thickness (1.8 mm) for AA5052-H32 and cold-rolled mild steel. Their findings indicated that the joints with steel as the upper sheet exhibited a higher static lap shear strength, whereas the joints with steel as the lower sheet demonstrated better fatigue resistance. Mori et al. explored the feasibility of joining ultra-high-strength steel to an aluminum alloy using SPR [22]. They discovered that if the rivet was not sufficiently hard, defects such as rivet fracture, rivet compression, and rivet bending could occur. Such defects typically arise when the rivet hardness is insufficient relative to the joined materials. By optimizing the rivet and die, they successfully joined SPFC980 ultrahigh-strength steel to AA5052-H34. Similarly, Hoang et al. observed rivet failures due to compression and fracture during the riveting process when aluminum alloys were joined using aluminum rivets [9].

Although previous studies examined specific material combinations [8, 21, 22] and stacking sequences [9], systematic understanding of how lower-sheet strength variations influence joint formation remains limited. Chung and Kim [21] and Mori et al. [22] demonstrated that relative sheet strength significantly affects rivet penetration and interlock development, yet these investigations were restricted to discrete material pairings rather than controlled strength variations.

To address this gap, the present study employs FE simulations to systematically elucidate how lower-sheet mechanical strength governs SPR joint formation. By fixing the upper sheet as AA7075-F and varying only the lower-sheet strength across three industrial alloys and two virtual materials, a controlled strength spectrum isolates the mechanical contribution of the lower sheet. This framework enables a mechanistic understanding of the strength–ductility balance required for effective rivet penetration, leg expansion, and stable interlock formation, providing guidance for optimal material selection in multi-material SPR applications. The remainder of this paper is organized as follows: section 2 outlines the SPR process, section 3 describes the FE modeling framework, section 4 presents numerical results and discussion, and section 5 concludes with key findings and implications.

2. SELF-PIERCING RIVETING PROCESS

2.1. Process description

The SPR process consists of four sequential stages [2, 3]: clamping, piercing, flaring, and releasing, as shown in Fig. 1. Initially, the blank-holder secures the sheet stack while the punch drives the rivet through the upper sheet. The rivet then penetrates into the lower sheet, where its legs expand radially within the die cavity to form a mechanical interlock. Finally, the punch retracts, leaving a robust joint without thermal distortion or pre-drilled holes [2, 3, 5].

Joint quality is governed by rivet geometry (shape, length, diameter), material properties (strength, ductility), punch force, and interfacial friction [16-18]. Proper parameter selection ensures adequate rivet expansion while preventing excessive thinning or premature fracture.

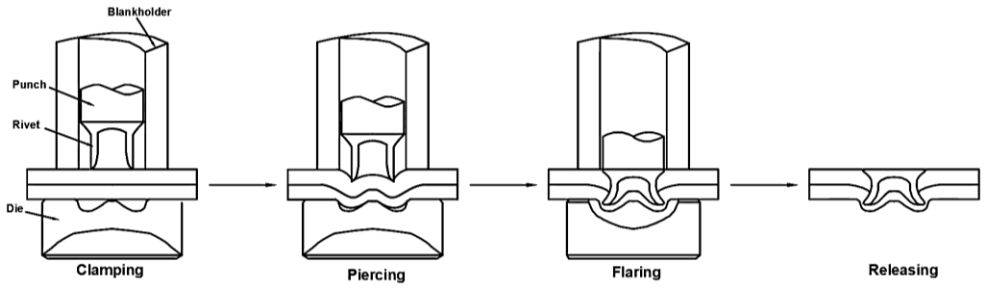

Figure 1. *Schematic diagram of the SPR process stages.*

2.2. Failure mechanisms in SPR joints

Despite its advantages, SPR joints may fail due to insufficient interlock formation, excessive sheet deformation, or fracture initiated by high stress concentration near the rivet–sheet interface [23-25]. Insufficient plastic deformation in the lower sheet can lead to rivet pullout, while poor material compatibility or improper compression may cause sheet separation and reduced joint strength [23, 24].

The mechanical properties of the joined sheets play a decisive role in joint formation and integrity [8, 21, 26]. During SPR, the lower sheet must simultaneously resist rivet penetration and accommodate sufficient plastic deformation to enable rivet-leg expansion. Overly soft substrates tend to deform excessively, promoting thinning or tearing before a stable interlock is formed, whereas excessively hard substrates restrict plastic flow and suppress leg flaring, thereby reducing interlock quality and joint stability under service loading [23, 26]. Achieving an appropriate balance between the strength and ductility of the lower sheet is therefore essential for reliable SPR joint formation and constitutes the focus of the present study.

3. FINITE ELEMENT MODEL

3.1. Material properties

This study examines five stacking configurations with a fixed upper sheet (AA7075-F, 2.1 mm) and varied lower sheet materials (1.5 mm thickness), as summarized in table 1. The rivet is U1500 steel, ensuring sufficient strength for penetration and leg expansion [6]. BA0270 serves as the baseline alloy, from which two virtual materials (Mat A and Mat B) are generated by adjusting flow stress by ±20%, enabling controlled examination of lower-sheet strength effects.

The mechanical response of materials in the SPR process is modeled using an elasto-plastic framework with isotropic hardening [6]. Plastic behavior is governed by a combination of the Swift and Voce hardening laws (denoted by CSV law) as follows:

$$\sigma_y(\bar{\varepsilon}) = \alpha A(\bar{\varepsilon} + \varepsilon_0)^n + (1 - \alpha)(k_0 + Q(1 - \exp^{-\beta\bar{\varepsilon}})) \quad (1)$$

where A, ε_0, and n define the Swift hardening components; k_0 ,Q, and β characterize the Voce hardening behavior; $\sigma_y(\bar{\varepsilon})$ denotes the reference flow stress. The weighting factor α controls the contribution of each component, and ε represents the equivalent plastic strain [27].

The onset of plastic deformation is defined using the von Mises yield criterion as follows:

$$F = \bar{\sigma}(\boldsymbol{\sigma}) - \sigma_y = \sqrt{\frac{3}{2}s_{ij}s_{ij}} - \sigma_y \leq 0 \quad (2)$$

where s_{ij} denotes the deviatoric stress tensor.

Previous studies have demonstrated that the Combined Swift–Voce (CSV) hardening law accurately captures the long-term strain hardening behavior of automotive sheet metals, making it

suitable for SPR simulations [6, 19, 28]. Fig. 2a presents the flow curves of the investigated materials calibrated using this model based on reference data [6]. For the virtual materials Mat A and Mat B, the same hardening formulation was retained while adjusting the strength level to systematically extend the material response range. This approach enables isolating the effect of lower-sheet strength on rivet deformation and interlock formation, which constitutes the primary objective of the present study.

Table 1. *Upper and lower sheet configurations for different cases.*

Component	Case				
	1	2	3	4	5
Upper sheet	AA7075-F	AA7075-F	AA7075-F	AA7075-F	AA7075-F
Lower sheet	AA2019	BA0270	AA7075-F	Mat A	Mat B

Table 2. *Material properties of the rivet, upper, and lower sheets [6].*

Part	Material	E (GPa)	Density (kg/m3)	Poisson's ratio
Rivet	U1500	220	7850	0.3
	AA2019	69	2780	0.33
	AA7075-F	72	2780	0.33
Sheet	BA0270	191	7850	0.3
	Mat A	191	7850	0.3
	Mat B	191	7850	0.3

Failure prediction is critical for SPR simulations due to the severe deformation and potential cracking at rivet-sheet interfaces. Among available approaches—including GISSMO [13], GTN porous-plasticity [12], and ductile fracture criteria [25, 29]—this study employs the Hosford–Coulomb model [28] owing to its validated accuracy for aluminum alloys under high triaxiality and large strains characteristic of cold forming and mechanical joining [10, 25, 29].

Table 3. *CSV hardening parameters of the materials.*

Material	α	A	ε_0	n	k_0	Q	β
U1500	0.973	1565.784	0.000004	0.0116	132.381	6227.87	145.719
AA7075-F	0.948	314.273	0.065	0.0607	25.401	2085.488	139.802
AA2019	0.939	710.201	0.225	0.1512	282.546	282.546	9.45
BA0270	0.434	882.856	0.01	0.4474	417.710	104.995	16.962
Mat A	0.423	1094.180	0.01	0.4424	486.924	122.233	17.012
Mat B	0.439	702.311	0.01	0.4424	334.076	83.864	17.012

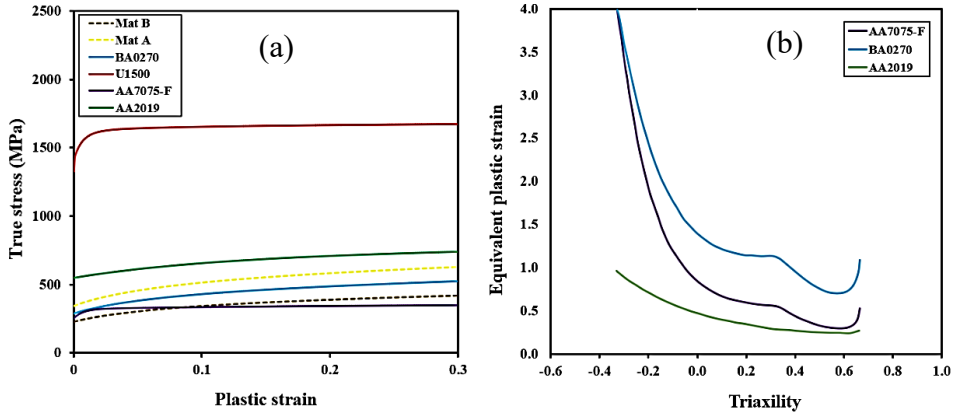

Figure 2. *(a) True stress - plastic strain curves of the investigated materials; (b) Hosford-Coulomb fracture curves of the tested materials [6].*

Damage accumulation follows the rate-independent formulation:

$$D = \int_0^{\bar{\varepsilon}_f} \frac{\mathrm{d}\bar{\varepsilon}}{\bar{\varepsilon}_f(\eta, \theta)} \tag{3}$$

where D is the damage indicator (fracture occurs at D = 1) and $\bar{\varepsilon}$ is the equivalent plastic strain. The fracture strain $\bar{\varepsilon_f}$ depends on stress triaxiality η and Lode angle parameter θ to capture multiaxial stress states typical of SPR forming [13, 26, 29]. Stress triaxiality is defined from the hydrostatic and von Mises stresses as:

$$\eta = \frac{tr(\boldsymbol{\sigma})/3}{\bar{\sigma}} \tag{4}$$

where $\mathrm{tr}(\boldsymbol{\sigma})/3$ is the hydrostatic stress and $\bar{\sigma}$ is the von Mises equivalent stress. The Lode-angle parameter is given by the normalized expression [28]:

$$\theta = 1 - \frac{2}{\pi}\arccos\left(\frac{27\det(s)}{2\bar{\sigma}^3}\right) \tag{5}$$

where s is the stress tensor and $\det(s)$ is its determinant. The parameter θ encodes the effect of the third invariant of the deviatoric stress on the fracture strain, and is constrained to $-1 \leq \theta \leq 1$ [28].

Model parameters from [6] were applied consistently across all materials (Fig. 2b). Mat A and Mat B adopted BA0270's fracture characteristics, ensuring that observed differences in joint formation arise solely from strength variations rather than damage tolerance [25].

3.2. Numerical model

An axisymmetric FE model was developed in Abaqus/Explicit to simulate the SPR process efficiently. The model includes six components: rivet, punch, upper sheet, lower sheet, die, and blank-holder (Fig. 3). The die and blank-holder are rigid bodies with encastre boundary conditions. The punch, also rigid, applies 5 mm displacement along the negative Y-axis to drive riveting. The rivet and sheets are deformable bodies capturing plastic flow and damage.

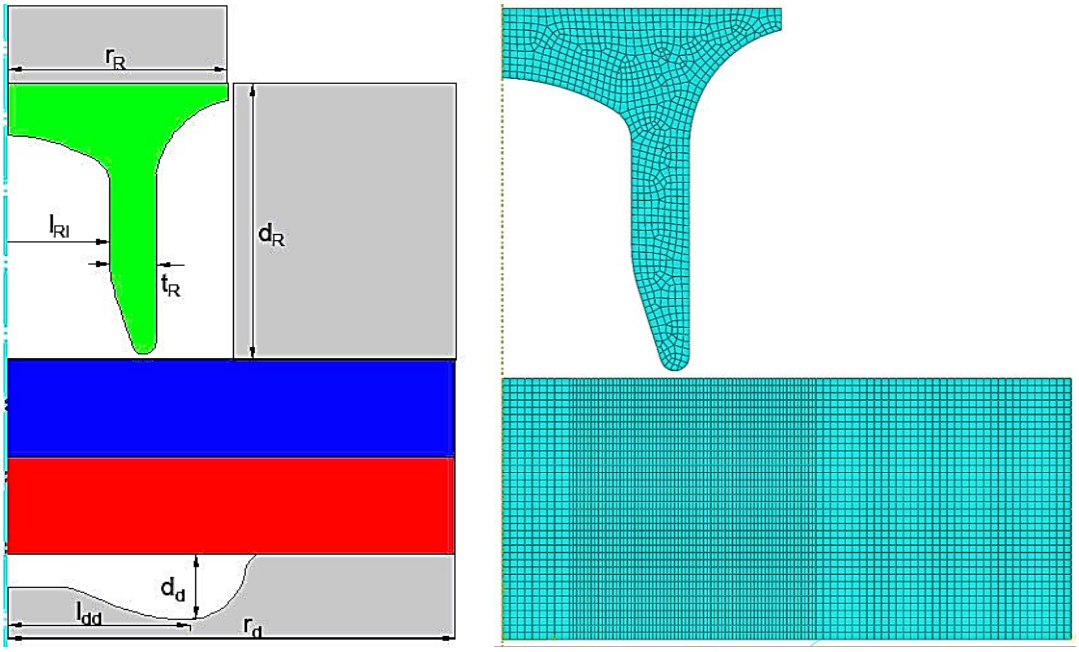

(a) *(b)*

Figure 3. *Modeling of the SPR process (a) Model geometries and (b) Mesh on the deformable parts.*

Table 4. *Geometric parameters of the die and rivet.*

Parameter	r_D	d_d	l_{dd}	d_R	r_R	t_R	l_{RI}
Value (mm)	7.85	1.2	3.2	5	3.85	0.8	1.78

Contact interactions use a general contact algorithm with Coulomb friction (μ = 0.1), typical for aluminum-steel cold forming [7, 28]. Kinematic contact formulation ensures robust constraint enforcement at rivet-sheet interfaces under large deformations.

Mesh refinement balances accuracy and efficiency (Fig. 3b). The rivet uses CAX4R and CAX3 elements with 0.1 mm size to capture stress gradients near the tip and legs. Both sheets employ CAX4R elements with 0.1 mm global size and 0.05 mm local refinement in high-strain zones near rivet penetration, accurately representing plastic deformation and potential cracking while optimizing computational cost.

4. RESULTS AND DISCUSSION

The results of the numerical simulations are presented and discussed in this section, beginning with the validation of the FE model against experimental data, followed by a detailed analysis of the joining response for different lower-sheet materials. The influence of material strength on force–displacement behavior, damage initiation, interlock development, and overall joint quality is systematically evaluated. By combining both global responses (e.g., force evolution) and local deformation characteristics (e.g., interlock, remaining thickness), the section clarifies the underlying mechanisms governing joint formation and highlights material-dependent trends essential for selecting suitable lower sheets in SPR applications.

4.1. Validation of the FE model

To validate the modeling approach, a FE simulation of an AA7075-F/BA0270 SPR joint was performed with sheet thicknesses of 2.1 mm and 1.5 mm, respectively, following [6]. Fig. 4a compares the predicted force–displacement response with experimental data. The simulation accurately reproduces the experimental trend across all stages—clamping, piercing, and flaring—with nearly identical slopes and load transitions. The predicted peak force of 63.0 kN shows good agreement with the experimental value of 65.2 kN, yielding a relative error of 3.4%, which is well within the acceptable range for SPR simulations. This close agreement confirms that the implemented material and contact models reliably capture the SPR mechanics.

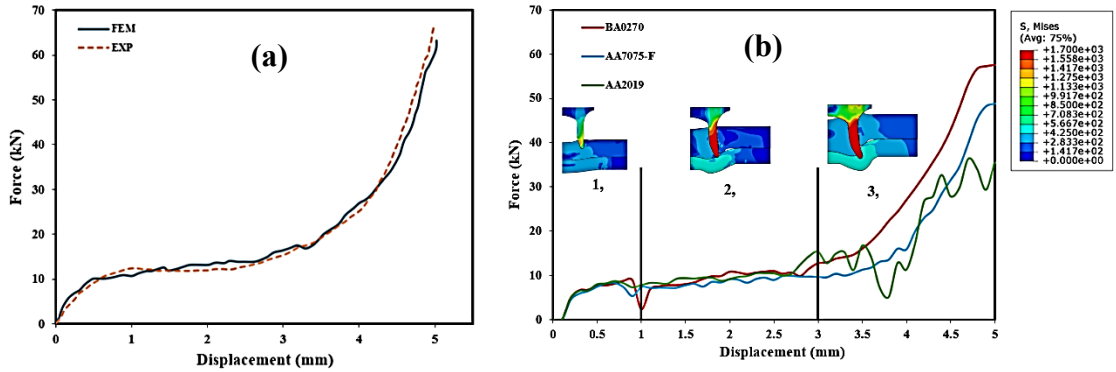

Figure 4. *(a) Comparison between experimental and FEM-predicted force–displacement curves for model validation, and (b) force–displacement responses of different lower-sheet materials during the SPR process.*

4.2. Evaluation of joining quality

Fig. 4b summarizes the global and local mechanical responses of the SPR process for the three real material systems. The force–displacement curves exhibit the characteristic three-stage

evolution of clamping, piercing, and flaring, in agreement with previous studies [2, 6, 14]. While the clamping and piercing stages show nearly identical responses due to the fixed AA7075-F upper sheet, clear divergence appears during the flaring stage, where deformation is governed by the lower sheet.

In this stage, BA0270 and AA2019 exhibit a steep force increase, indicating sufficient confinement for rivet-leg expansion. However, AA2019 shows pronounced force oscillations associated with localized strain accumulation and the onset of brittle cracking under a highly triaxial stress state. In contrast, AA7075-F displays a flatter force response with a reduced peak load, reflecting early softening and insufficient lateral resistance, which promotes excessive downward flow and premature tearing. Only BA0270 is observed to maintain a stable force increase without damage localization, demonstrating a balanced combination of strength and deformability that supports controlled rivet-leg expansion and stable interlock formation, consistent with reported SPR behavior for ductile substrates [14, 21].

The damage contours in Fig. 5 further clarify the distinct failure mechanisms of the lower-sheet materials. In AA2019, damage localizes rapidly beneath the rivet leg, forming a narrow fracture band that leads to brittle cracking at an early stage of flaring. In contrast, AA7075-F exhibits a more diffuse damage distribution accompanied by pronounced thinning, which ultimately results in a tearing-type failure. By comparison, BA0270 shows no significant damage localization, indicating a stable deformation regime and superior resistance to fracture during rivet-leg expansion.

Overall, the combined force response and damage evolution indicate that AA2019 fails due to limited ductility, AA7075-F fails due to over-softening, and BA0270 appears to provide the most balanced mechanical conditions required for successful rivet-leg expansion. Consequently, BA0270 is selected as the reference material for the subsequent parametric investigation using the virtual materials Mat A and Mat B.

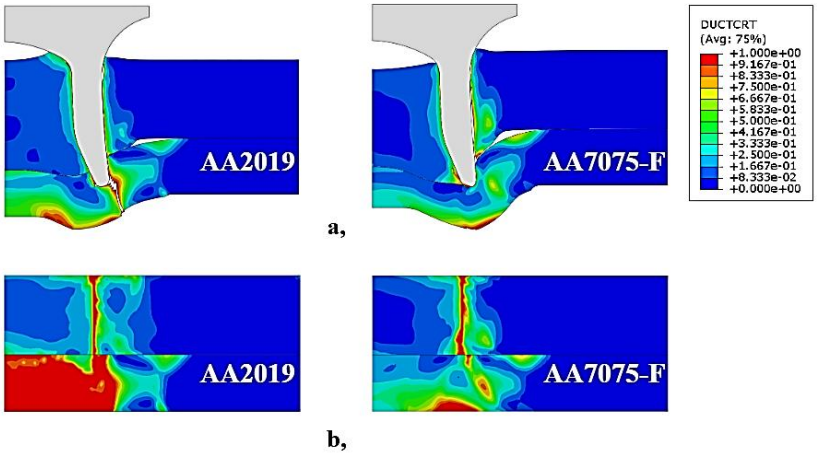

Figure 5. *Comparison of damage initiation and damage distribution in AA2019 and AA7075-F lower sheets during SPR: (a) onset of fracture and (b) undeformed state after damage evolution.*

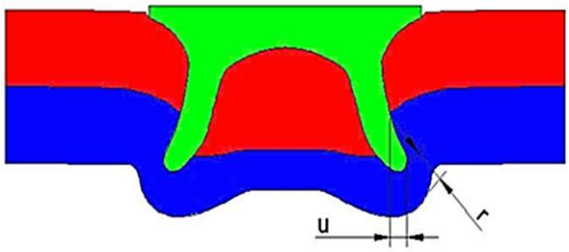

Figure 6. *Characterization of a SPR joint: interlock length (u) and remaining thickness (r).*

4.3. Influence of the lower sheet strength on the joint quality

Having established BA0270 as the only real material capable of forming a fracture-free joint, two virtual materials—Mat A and Mat B—were introduced by increasing and decreasing the flow-stress level of BA0270 by ±20% to isolate the effect of lower-sheet strength. For the three non-failing cases (BA0270, Mat B, and Mat A), joint quality is evaluated using the interlock length (u) and remaining thickness (r), as defined in Fig. 6, which are widely accepted joinability indices [3, 9].

The deformation fields in Fig. 7 show that interlock formation is governed by the deformation mode of the lower sheet. For BA0270, the von Mises stress and equivalent plastic strain fields are broadly distributed around the rivet leg, indicating stable plastic flow that accommodates rivet penetration while providing sufficient lateral resistance for rivet-leg expansion. This balanced response results in the largest interlock (0.32 mm) together with a favorable remaining thickness (0.64 mm).

In contrast, Mat B exhibits extensive plastic deformation concentrated beneath the rivet tip. The PEEQ contours indicate dominant downward material flow accompanied by pronounced thinning, which limits effective lateral confinement. As a result, although Mat B still forms a comparable interlock (0.29 mm), the remaining thickness decreases to 0.60 mm, reflecting an over-softened response consistent with the limitations of low-strength substrates in SPR joints [9].

Mat A shows the opposite behavior. Increased strength leads to stress localization and limited plastic strain accumulation around the rivet leg, while elevated triaxiality indicates a highly constrained stress state. This suppresses rivet-leg rotation and outward expansion, resulting in the smallest interlock (0.25 mm) despite preserving the greatest remaining thickness (0.81 mm). Such stress-induced stiffening is commonly observed in high-strength alloys under confined loading conditions [3, 9, 26].

Taken together, the deformation fields and joinability indices in Fig. 7 define two limiting deformation regimes: excessive downward flow with insufficient confinement in Mat B, and excessive constraint with restricted plastic flow in Mat A. Only BA0270 exhibits a balanced deformation response, in which plastic flow and lateral resistance are properly coupled to promote stable rivet-leg expansion. This confirms that effective SPR joinability depends not simply on lower-sheet strength, but on achieving an appropriate balance between plastic deformability and confinement during the interlock-formation stage.

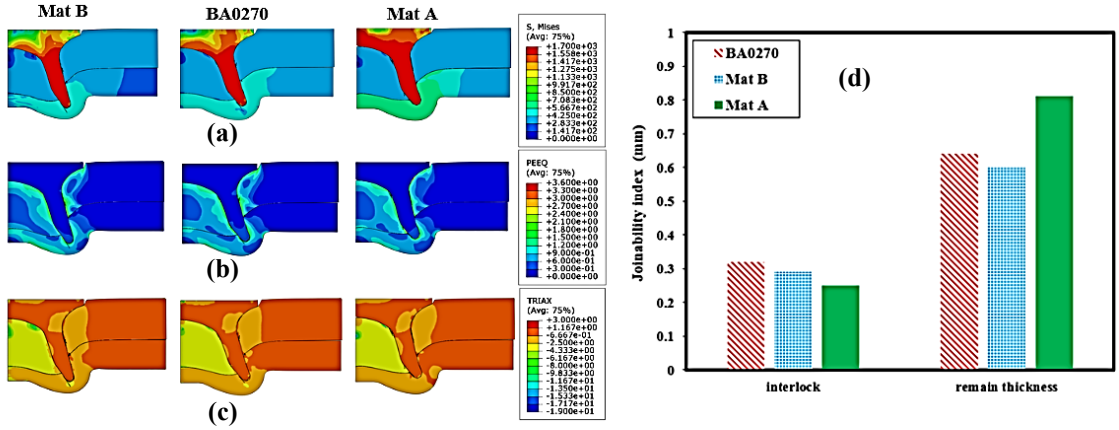

Figure 7. *Distributions of (a) von Mises stress, (b) equivalent plastic strain, and (c) stress triaxiality for Mat B, BA0270, and Mat A at the final interlock-formation stage, together with (d) the corresponding joinability indices.*

5. CONCLUSIONS

This study clarified how the mechanical properties of the lower sheet govern the deformation pathway and joinability of SPR joints. The force–displacement behavior and damage evolution showed that AA2019 fails due to insufficient ductility, whereas AA7075-F fails due to excessive softening. BA0270 is the only real material that enables stable rivet-leg expansion without fracture, making it a suitable reference for further material exploration.

By introducing two virtual materials offset ± 20% in strength relative to BA0270, the analysis revealed a clear strengthening–softening trade-off. Softer materials promote penetration but suffer from excessive thinning, while stronger materials suppress rivet-leg expansion. The joinability indices, interlock length and remaining thickness, demonstrate that only materials with intermediate strength achieve a favorable balance between confinement and deformability. BA0270 sits closest to this optimal window.

These findings emphasize that lower-sheet strength should be carefully balanced to ensure both adequate rivet penetration and effective interlock formation. The insights gained here provide a mechanistic basis for material selection and offer a practical framework for virtual material screening in SPR joint design.

Acknowledgement: *This research is funded by Vietnam National Foundation for Science and Technology Development (NAFOSTED) under grant number NCUD.01-2025.25. The authors would like to thank Dr. Lun Zhao from Institute of Ultrasonic Technology, Shenzhen Polytechnic University, China for enthusiastic and valuable discussions.*

REFERENCES

[1]. Czerwinski, F., *"Current Trends in Automotive Lightweighting Strategies and Materials"*, Materials, Vol. 14, No. 21, Article 6631, (2021).

[2]. Chrysanthou, A.; Sun, X., *"Self-piercing Riveting: Properties, Processes and Applications"*, Woodhead Publishing, (2014).

[3]. Li, D.; Chrysanthou, A.; Patel, I.; Williams, G., *"Self-piercing riveting – a review"*, International Journal of Advanced Manufacturing Technology, Vol. 92, pp. 1777–1824, (2017).

[4]. Ang, H. Q., *"An overview of self-piercing riveting process with focus on joint failures, corrosion issues and optimisation techniques"*, Chinese Journal of Mechanical Engineering, Vol. 34, No. 1, Article 2, (2021).

[5]. He, X.; Pearson, I.; Young, K., *"Self-pierce riveting for sheet materials: state of the art"*, Journal of Materials Processing Technology, Vol. 199, No. 1–3, pp. 27–36, (2008).

[6]. Karathanasopoulos, N.; Pandya, K. S.; Mohr, D., *"An experimental and numerical investigation of the role of rivet and die design on the self-piercing riveting joint characteristics of aluminum and steel sheets"*, Journal of Manufacturing Processes, Vol. 69, pp. 290–302, (2021).

[7]. Yang, B.; Ma, Y.; Shan, H.; Niu, S.; Li, Y., *"Friction self-piercing riveting (F-SPR) of aluminum alloy to magnesium alloy using a flat die"*, Journal of Magnesium and Alloys, Vol. 10, No. 5, pp. 1207–1219, (2022).

[8]. Abe, Y.; Kato, T.; Mori, K., *"Joinability of aluminium alloy and mild steel sheets by self piercing rivet"*, Journal of Materials Processing Technology, Vol. 177, No. 1–3, pp. 417–421, (2006).

[9]. Hoang, N.-H.; Porcaro, R.; Langseth, M.; Hanssen, A.-G., *"Self-piercing riveting connections using aluminium rivets"*, International Journal of Solids and Structures, Vol. 47, No. 3–4, pp. 427–439, (2010).

[10]. Amer, M.; Shazly, M.; Mohamed, M.; Hegazy, A. A., *"Ductile damage prediction of AA5754 sheet during cold forming condition"*, Journal of Mechanical Science and Technology, Vol. 34, pp. 4219–4228, (2020).

[11]. Bai, Y.; Wierzbicki, T., *"Application of extended Mohr–Coulomb criterion to ductile fracture"*, International Journal of Fracture, Vol. 161, No. 1, pp. 1–20, (2010).

[12]. Ji, H.; Ma, Z.; Huang, X.; Xiao, W.; Wang, B., *"Damage evolution of 7075 aluminum alloy based on the Gurson–Tvergaard–Needleman model under high temperature conditions"*, Journal of Materials Research and Technology, Vol. 16, pp. 398–415, (2022).

[13]. Otroshi, M.; Rossel, M.; Meschut, G., *"Stress state dependent damage modeling of self-pierce riveting process simulation using GISSmo damage model"*, Journal of Advanced Joining Processes, Vol. 1, Article 100015, (2020).

[14]. Rusia, A.; Weihe, S., *"Development of an end-to-end simulation process chain for prediction of self-piercing riveting joint geometry and strength"*, Journal of Manufacturing Processes, Vol. 57, pp. 519–532, (2020).

[15]. Ma, Y.; Li, Y.; Hu, W.; Lou, M.; Lin, Z., *"Modeling of friction self-piercing riveting of aluminum to magnesium"*, Journal of Manufacturing Science and Engineering, Vol. 138, No. 6, Article 061007, (2016).

[16]. Uhe, B.; Kuball, C.-M.; Merklein, M.; Meschut, G., *"Improvement of a rivet geometry for the self-piercing riveting of high-strength steel and multi-material joints"*, Production Engineering, Vol. 14, pp. 417–423, (2020).

[17]. Zhao, L.; He, X.; Xing, B.; Lu, Y.; Gu, F.; Ball, A., *"Influence of sheet thickness on fatigue behavior and fretting of self-piercing riveted joints in aluminum alloy 5052"*, Materials & Design, Vol. 87, pp. 1010–1017, (2015).

[18]. Abe, Y.; Kato, T.; Mori, K., *"Self-piercing riveting of high tensile strength steel and aluminium alloy sheets using conventional rivet and die"*, Journal of Materials Processing Technology, Vol. 209, No. 8, pp. 3914–3922, (2009).

[19]. Kim, C.; Min, K. M.; Choi, H.; Kim, H. J.; Lee, M.-G., *"Development of analytical strength estimator for self-piercing rivet joints through observation of finite element simulations"*, International Journal of Mechanical Sciences, Vol. 202, Article 106499, (2021).

[20]. Mori, K.; Abe, Y.; Kato, T., *"Self-pierce riveting of multiple steel and aluminium alloy sheets"*, Journal of Materials Processing Technology, Vol. 214, No. 10, pp. 2002–2008, (2014).

[21]. Chung, C.-S.; Kim, H.-K., *"Fatigue strength of self-piercing riveted joints in lap-shear specimens of aluminium and steel sheets"*, Fatigue & Fracture of Engineering Materials & Structures, Vol. 39, No. 9, pp. 1105–1114, (2016).

[22]. Mori, K.; Kato, T.; Abe, Y.; Ravshanbek, Y., *"Plastic joining of ultra high strength steel and aluminium alloy sheets by self piercing rivet"*, CIRP Annals, Vol. 55, No. 1, pp. 283–286, (2006).

[23]. Mucha, J., *"The failure mechanics analysis of the solid self-piercing riveting joints"*, Engineering Failure Analysis, Vol. 47, pp. 77–88, (2015).

[24]. Han, L.; Chrysanthou, A.; Young, K., *"Mechanical behaviour of self-piercing riveted multi-layer joints under different specimen configurations"*, Materials & Design, Vol. 28, No. 7, pp. 2024–2033, (2007).

[25]. Hönsch, F.; Domitner, J.; Sommitsch, C.; Götzinger, B., *"Modeling the failure behavior of self-piercing riveting joints of 6xxx aluminum alloy"*, Journal of Materials Engineering and Performance, Vol. 29, pp. 4888–4897, (2020).

[26]. Uhe, B.; Meschut, G., *"Advanced self-piercing riveting of ultra-high-strength steel through rivets with modified material properties"*, Journal of Manufacturing Processes, Vol. 125, pp. 354–363, (2024).

[27]. Pham, Q. T.; Kim, Y.-S., *"Evaluation on flexibility of phenomenological hardening law for automotive sheet metals"*, Metals, Vol. 12, No. 4, Article 578, (2022).

[28]. Mohr, D.; Marcadet, S. J., *"Micromechanically-motivated phenomenological Hosford–Coulomb model for predicting ductile fracture initiation at low stress triaxialities"*, International Journal of Solids and Structures, Vol. 67, pp. 40–55, (2015).

[29]. Rusia, A.; Beck, M.; Weihe, S., *"Simulation of self-piercing riveting process and joint failure with focus on material damage and failure modelling"*, Proceedings of the 12th European LS-DYNA Conference, Koblenz, Germany, (2019).

TÓM TẮT

Ảnh hưởng của vật liệu tấm dưới đến chất lượng mối ghép bằng đinh tán tự đâm xuyên

Đinh tán tự đâm xuyên (SPR) đã trở thành một phương pháp ghép nối quan trọng trong các kết cấu nhẹ nhưng yêu cầu độ bền cao, đặc biệt trong ngành công nghiệp ô tô và hàng không vũ trụ. Nghiên cứu này tập trung đánh giá ảnh hưởng của độ bền tấm dưới đến chất lượng mối ghép SPR. Để đạt được mục tiêu đó, tấm trên được giữ cố định trong mọi trường hợp, trong khi tấm dưới được thay đổi với các vật liệu khác nhau (AA7075-F, AA2019, BA0270, Mat A và Mat B). Một mô hình phần tử hữu hạn trong Abaqus/Explicit được xây dựng nhằm mô phỏng quá trình ghép và phân tích chất lượng mối ghép. Các chỉ tiêu đánh giá chính bao gồm độ khóa liên kết, độ dày còn lại và vị trí đầu đinh tán. Kết quả cho thấy tấm dưới cần đạt một mức độ bền tối thiểu để hình thành mối ghép hoàn chỉnh. Tuy nhiên, khi tấm dưới quá cứng, sự kháng biến dạng quá lớn sẽ hạn chế quá trình loe chân đinh tán, làm giảm khả năng hình thành khóa liên kết mặc dù đinh tán vẫn xuyên qua được tấm trên.

Từ khóa: Đinh tán tự đâm xuyên; Phân tích phân tử hữu hạn; Chất lượng mối ghép; Kim loại tấm; Vật liệu ảo.